Research Article | Vol. 11, No. 6 / 1 June 2020 / Biomedical Optics Express 3246
Biomedical Optics EXPRESS

Novel quantitative signature of tumor stromal architecture: polarized light imaging differentiates between myxoid and sclerotic human breast cancer stroma

BLAKE JONES,[1,6] GEORGIA THOMAS,[1,6] JARED WESTREICH,[1] SHARON NOFECH-MOZES,[2] ALEX VITKIN,[1,3,4,7,*] AND MOHAMMADALI KHORASANI[5,7]

[1]*Department of Medical Biophysics, University of Toronto, 101 College St, Toronto, ON M5G 1L7, Canada*
[2]*Department of Laboratory Medicine and Pathobiology, University of Toronto, 1 King's College Cir, Toronto, ON M5S 1A8, Canada*
[3]*Division of Biophysics and Bioimaging, Princess Margaret Cancer Center, University Health Network, 610 University Ave, Toronto, ON M5G 2C1, Canada*
[4]*Department of Radiation Oncology, University of Toronto, Stewart building, 149 College St Suite 504, Toronto, ON M5 T 1P5, Canada*
[5]*Department of Surgical Oncology, University of Toronto, Princess Margaret Cancer Center, OPG Wing, 6th floor, 610 University Avenue Toronto, ON M5G 2M9, Canada*
[6]*Authors contributed equally*
[7]*Co-senior authors*
[*]*Alex.Vitkin@rmp.uhn.ca*

Abstract: As a leading cause of death in women, breast cancer is a global health concern for which personalized therapy remains largely unrealized, resulting in over- or under-treatment. Recently, tumor stroma has been shown to carry important prognostic information, both in its relative abundance and morphology, but its current assessment methods are few and suboptimal. Herein, we present a novel stromal architecture signature (SAS) methodology based on polarized light imaging that quantifies patterns of tumor connective tissue. We demonstrate its ability to differentiate between myxoid and sclerotic stroma, two pathology-derived categories associated with significantly different patient outcomes. The results demonstrate a 97% sensitivity and 88% specificity for myxoid stroma identification in a pilot study of 102 regions of interest from human invasive ductal carcinoma breast cancer surgical specimens (20 patients). Additionally, the SAS numerical score is indicative of the wide range of stromal characteristics within these binary classes and highlights ambiguous mixed-morphology regions prone to misclassification. The enabling polarized light microscopy technique is inexpensive, fast, fully automatable, applicable to fresh or embedded tissue without the need for staining and thus potentially translatable into research and/or clinical settings. The SAS metric yields quantifiable and objective stromal characterization with promise for prognosis in many types of cancers beyond breast carcinoma, enabling researchers and clinicians to further investigate the emerging and important role of stromal architectural patterns in solid tumors.

1. Introduction

Breast cancer is the most common cause of oncologic mortality in women, with over 600,000 people succumbing to the disease in 2018 worldwide [1]. The condition encompasses a heterogeneous group of malignancies with a variety of locoregional behavior and distant metastatic potential. This inherent variance in aggressiveness and outcomes calls for additional markers to help personalize treatment strategies and minimize over- or under-treatment of patients

#392722 https://doi.org/10.1364/BOE.392722
Journal © 2020 Received 16 Mar 2020; revised 12 May 2020; accepted 14 May 2020; published 21 May 2020

Biomedical Optics EXPRESS

[2,3]. Current efforts in the search for additional prognostication markers are primarily focused on molecular and genetic characteristics of the tumors and their host environment. Several of these assays, such as Oncotype Dx (Genomic Health Inc, USA), Prosigna (NanoString Technologies Inc, USA) and EndoPredict (Myriad Genetics Inc, Switzerland), have yielded some advancements in predicting recurrence risk in a subset of breast cancer patients [4]. However, these tests are expensive [5] and their clinical utility could be improved [6]. As a result, there exists a significant need for additional prognostic and predictive markers.

In addition to studying the cancer cells themselves, researchers have turned to the host environment milieu of the tumor, known as the tumor microenvironment (TME) [7] as a potential source of new biomarkers. The TME is composed of stroma, which is rich in various cellular, molecular and structural components. Collagen and fibrin fibers within the stroma facilitate the interplay of signaling pathways within the TME, and changes in their architectural patterns are believed to reflect interactions between the tumor and its host environment. Preliminary research has demonstrated that the amount of fibrillar stroma within the TME and the architectural patterns of its fibers are linked to tumor progression and treatment response [8–12].

Initial attempts to assess stromal prognosticative potential examined the relative amount of stroma and tumor, quantified via the tumor-stroma ratio (TSR). Increased fractional stromal volume was linked to less favorable patient outcomes, such as shorter relapse-free periods and increased patient mortality, even amongst different molecular subtypes of breast cancer [13–17]. Similar correlations have been found in several other solid tumors beyond breast cancer [18–20], demonstrating the potentially important prognostic information of the relative abundance of stroma. In addition to the amount, the architectural patterns of stromal fibers and the morphology of their arrangements have been linked to prognosis [21–25]. Currently, a pathologist can qualitatively categorize tumoral stroma architecture as either myxoid or sclerotic. The former presents as sparse, unaligned chaotic collagen fibers in a basophilic amorphous material, while the latter is characterized by long, organized and often densely packed fibers resembling stromal patterns of normal tissues. The presence of myxoid stroma in the TME has been correlated with increased patient mortality and more aggressive pathology in a variety of diseases such as ductal carcinoma in situ (DCIS) [24], cholangiocarcinoma [22], pancreatic ductal adenocarcinoma [25] and rectal cancer [23].

While such TSR and binary stromal categorization methods show promising prognostic potential, both rely on microscopic evaluation of H&E stained slides by a pathologist. This process is subjective and difficult to reproduce, causing inevitable intra and inter-observer variability. In addition, the complex stromal morphology patterns are unlikely to be well captured by a simplistic binary myxoid versus sclerotic classification scheme. Improved assessment of the spectrum of stromal architecture thus calls for a reproducible, quantitative and continuous-scoring method to enable improved stromal characterization and realization of its full prognostic potential.

We propose a novel stromal architecture signature (SAS) based on polarized light microscopy (PLM) that quantitatively characterizes the stromal architecture and demonstrate its ability to differentiate between myxoid and sclerotic stroma in unstained human breast cancer specimens. Previous work has shown the ability of full Mueller matrix polarimetry to characterize breast cancer samples by stage [26]. However, our optical imaging relies on a simpler rotating-crossed-polarizers approach that yields measurement-geometry-independent images with excellent contrast of birefringent structures such as stromal fibers [27]. These are then fed into a robust image processing and statistical analysis pipeline to generate a quantitative signature of the spectrum of architectural patterns exhibited by tumoral stroma. In contrast to pathologist-based subjective assessments, polarimetric SAS methodology is quantitative and objective. On a practical note, the proposed technique is suitable for unstained (potentially fresh or non-fixed) tissues, is fast (~80,000 px/s, for example ~3 minutes for a 1.6×1.6 mm^2 area at 80x magnification) and is inexpensive. The method is thus directly implementable into most commercial microscopes and potentially

Biomedical Optics EXPRESS

into breast oncology clinical workflows and may be automated to avoid human/pathologist intervention. Owing to the recently reported prognostic importance of stromal morphology in many other solid tumors [22,23,25], broad biomedical applications beyond breast cancer are envisioned.

2. Methods

2.1. Ethics

Institutional ethics approval was obtained from participating hospital institutions (University Health Network and Sunnybrook Hospital, both in Toronto, Canada). The need for patients' consent to examine the breast cancer histopathology samples was waived by the ethics board due to the retrospective nature of the study and complete anonymization of personal health information.

2.2. Samples

Surgically removed specimens of invasive ductal carcinoma (IDC), the most common form of invasive breast cancer, from 20 patients with no prior chemotherapy or radiotherapy treatments were imaged using the PLM technique described below. The samples were unstained, formalin-fixed paraffin embedded and 4.5 μm thick. A variety of hormone receptor statuses were included. Prior to PLM imaging, the unstained samples were chemically dewaxed to reduce possible polarimetric signal artifacts [28]. Although the remaining formalin fixation can induce modest polarimetric changes due to cross-linking (of the order of 10-20% as we have quantified previously [28]), these will have limited effect on collagenous stroma contrast and the trends reported below. Adjacent histological slides were H&E stained and scanned using 20x magnification for pathologist assessment as the gold standard.

2.3. ROI selection and histology

From the 20 adjacent H&E slides, 102 regions of interest (ROI, 200μm x 200μm) containing tumor stroma were chosen. An experienced practicing pathologist blinded to the polarimetry results then labelled each ROI. The following categories and their respective criteria were used in the labelling: myxoid regions were defined as having over 33% myxoid stroma (n=33), sclerotic regions as having no evidence of myxoid stroma (n=48), and mildly myxoid as having both categories, but with less than 1/3 of the total ROI area exhibiting myxoid stroma (n=15). Regions corresponding to biopsy sites, hemorrhage or necrosis were excluded (n=6).

2.4. Polarimetric imaging

The unstained samples were imaged using an AxioZoom V16 microscope (Zeiss, Germany), chosen for its conveniently large working distance (5.4cm), with ample space for incorporating the rotating crossed polarizers into the imaging setup as shown in Fig. 1. Light was transmitted through the samples using a 310W LED (Illuminator HXP 200C (D), Zeiss, Germany) uncollimated white light source passing through a filter centered at 630 nm. As previously described, the simple optical setup consists of two crossed linear polarizers (Thorlabs, LPVISE100-A) on either side of the tissue sample [27]. The polarizers were controlled by two motorized rotation mounts (PRM1.MZ8, Thorlabs, USA) and rotated simultaneously while remaining perpendicular to each other. Images were taken at 18 different angular positions, equally spaced between 0 and 90°. For this study, the ROIs were imaged at 80x, with an approximate field of view of 1.6×1.6 mm^2 and resolution of 1.6μm. Images were also acquired without the sample to enable a flood field correction.

To understand the essence of the technique, note that linear polarizers only allow light of one linear orientation to pass. Thus, for two perpendicular linear polarizers with nothing in

Biomedical Optics EXPRESS

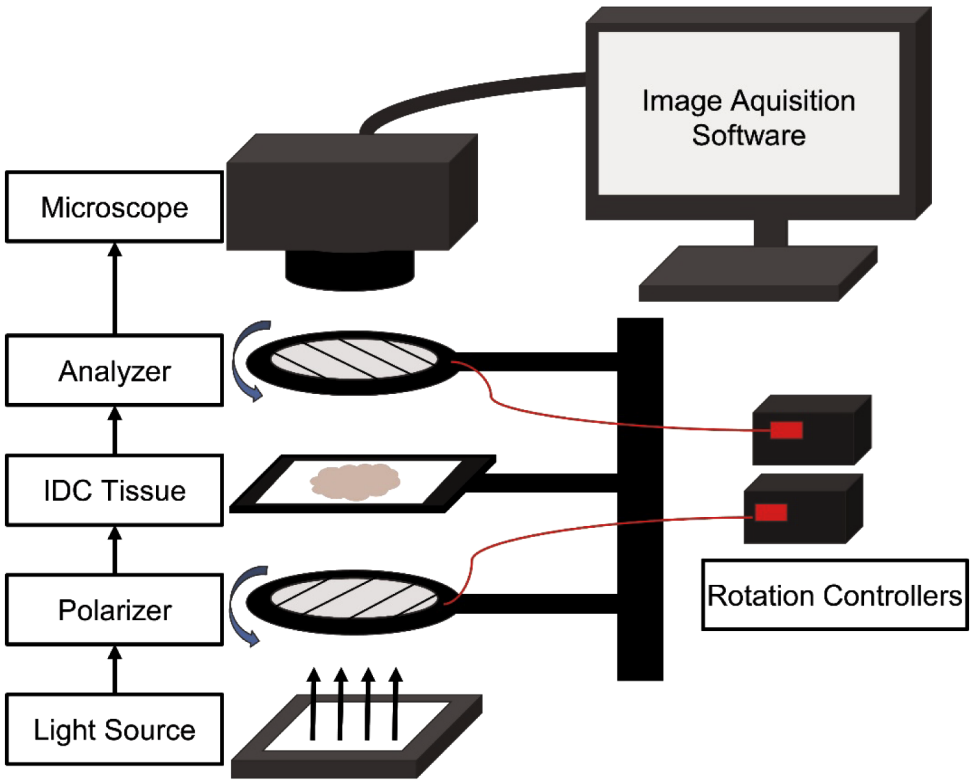

Fig. 1. Diagram of the PLM imaging system.

between, no light will pass through (to within the pair's extinction ratio). However, barring any other optical effects, if there is a birefringent material between the two polarizers, light will be transmitted with the following intensity:

$$Intensity = \sin^2\left(\frac{\Delta n \pi t}{\lambda}\right)\sin^2(2\tau) \tag{1}$$

where τ is the relative angle between the analyzer polarization direction and the birefringent axis of the material, Δn is its birefringence, t is its thickness and λ is the light wavelength. Since all values are kept constant over the different angular measurement positions, transmittance intensity of a birefringent structure will vary with measurement angle according to:

$$Intensity \propto \sin^2(2\tau) \tag{2}$$

with the maximum intensity occurring when $\tau = 45°$. This angular modulation of signal intensity is the important difference between this method and the conventional crossed-polarizers approaches. In these, the detected intensity depends on tissue birefringent properties, in particular their orientation, and on polarization optics orientation. In contrast, our method integrates out the uninteresting measurement geometry effects (as per Eq. (2)) and furnishes tissue-only intrinsic birefringent data. Specifically, signal processing over the different angular images allows determination of the measurement-geometry-independent tissue birefringence properties, namely its magnitude (first term of Eq. (1)) and orientation (second term) at each pixel. This simple yet robust approach yields high contrast information-rich polarimetric images that are further processed to furnish quantitative stromal metrics for pathology slide assessment.

Biomedical Optics EXPRESS

2.5. Image quantification

In order to distinguish between regions composed of myxoid and sclerotic stroma, to provide a continuous numeric score, and to develop the overall methodology, three individual metrics based on the three different derived images [Fig. 2(d), (e) and (f)] were calculated before being combined into a single composite. The metrics and their scores each seek to assess a particular morphologic or optical property posited to differentiate between the myxoid and sclerotic stroma based on their histopathological definition, namely: intensity that reflects the amount and thickness of fibers, alignment which captures the degree of their local organization, and density which measures how closely packed the fibers are. All metrics and their scores were determined from individual pixel-level values, thus enabling parametric images of each [Fig. 2(d), (e) and (f)]. The two former metrics have been previously described [27], and the third is introduced here to help improve stromal architecture quantification.

2.5.1. Intensity (Fig. 2(d))

The first derived image represents birefringent intensity. Birefringence is an optical property of asymmetric materials that have refractive indices dependent on the direction and polarization of incident light. Collagen is birefringent, and therefore the transmitted light intensity varies significantly with polarization measurement angle. Many other biological tissue types, including tumor cells, are much less birefringent, if at all; thus, the transmitted light is substantially less dependent on the measurement angle. The degree to which a particular region is birefringent was hypothesized to be directly proportional to the amount of collagenous stroma present. To capture this in a measurement-angle-independent image, the standard deviation of the light intensities across the different angular measurements was calculated to obtain the maximum intensity range (MIR),

$$MIR(i,j) \equiv \sqrt{\frac{\sum_{z=1}^{Z} \left(y_{(i,j,z)} - \bar{y}_{(i,j)}\right)^2}{z-1}} \tag{3}$$

where z is the number of images in the stack (18 in this study), $y_{(i,j,z)}$ indicates the brightness at a particular pixel (i,j) in a given angular image, z and $\bar{y}_{(i,j)}$ is the mean for all light intensity values at position (i,j).

Note that unlike any one particular angular image in a stack (Fig. 2(b)) where the local brightness depends on both tissue properties and polarization optics angle (see Eq. (1)), $MIR(i,j)$ and the resultant image of Fig. 2(d) are both polarization-angle-independent. Thus, the good contrast between tumor and stroma visible on such images is indicative of intrinsic tissue properties without the uninteresting admixture of the measurement system details. We posit that sclerotic stroma would result in higher MIR values than myxoid regions, due to its organized nature. In the ROI analysis below, the intensity metric is defined as the median MIR within the selected ROI.

2.5.2. Alignment (Fig. 2(e))

Another important characteristic in the classification of stroma is the alignment of collagen fibers. Myxoid stroma tends to have unaligned, randomly oriented chaotic collagen fibers while sclerotic stroma exhibits fibrillar structures that are more aligned with their neighbors. Analysis of the PLM angular image stack allows for the extraction of the optical axis, which in the case of collagenous stroma is the long axis of the fiber itself [27]. The birefringence orientation for every pixel was thus found by noting the angle of the polarizer which yielded the maximum in the curves of Fig. 2(c). The degree of alignment quantifies the distribution of these fiber orientations, whereby a 5×5 pixel sliding window was applied to the pixel-wise orientation image to calculate the mean angular difference (MAD) of the stromal directions. This window size was selected

Biomedical Optics EXPRESS

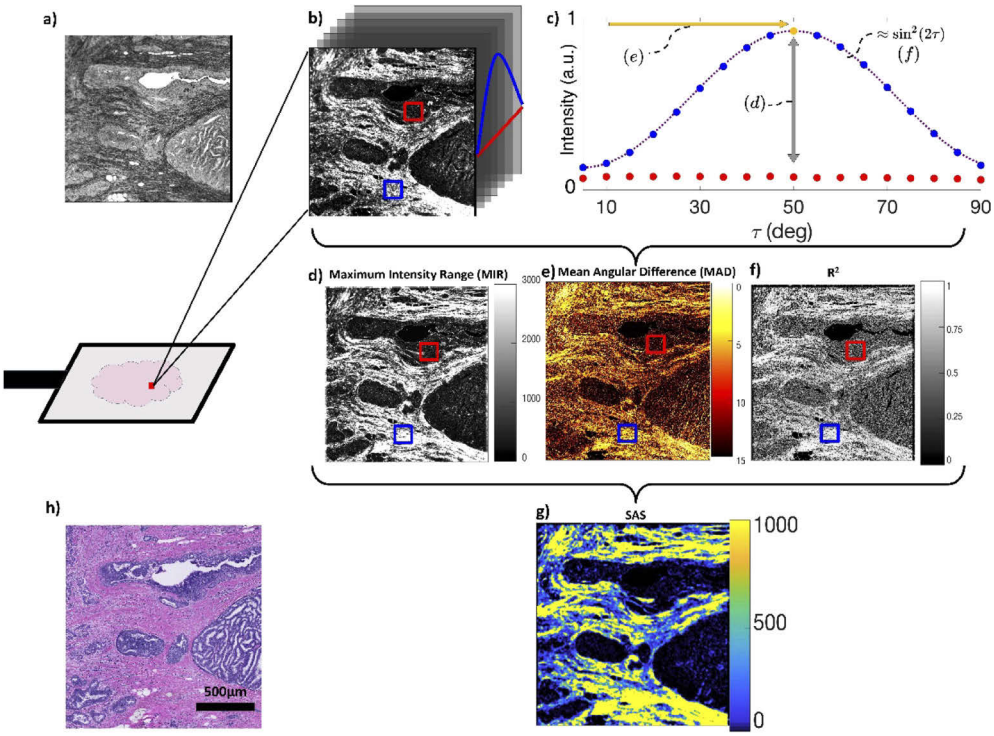

Fig. 2. Outline of the imaging and image analysis pipeline used to calculate the SAS. During the imaging phase, both a) White light image of unstained slide and b) PLM cross-polarized stack imaged at 18 angular increments of 5° between 0° and 90° are acquired. c) Light intensity pattern for pixels corresponding to birefringent and non-birefringent regions (blue and red symbols). The corresponding image regions from which these pixels were chosen are highlighted with blue and red squares in b), d), e) and f). The former exhibit an oscillating intensity pattern characteristic of a birefringent material while the latter, originating from less birefringent structures such as tumor cells, exhibit no significant angular intensity variation. The normalized theoretical intensity oscillation (Eq. (2)) is shown by the dotted-purple line. From these intensity curves, three parametric images are derived. d) Maximum Intensity Range (MIR) image, correlating with the maximum peak-to-trough height of curves in c) at each pixel, indicated by the grey arrow in c). e) Mean Angular Difference (MAD) image, where the intensity values are indicative of the mean difference in fiber directions over a 5×5 pixel sliding analysis window (fiber directions were calculated from the angular location of the maximum (indicated by the yellow arrow) in c). f) R^2 image, where the intensity values are indicative of the goodness-of-fit of c) to Eq. (2) (purple-dotted line in c)). g) SAS image, derived from the product of the three preceding images. Pixels corresponding to greater degree of stromal organization have higher SAS values indicated by lighter colors. h) In parallel, an adjacent H&E stained slide is scanned at 20X and registered with the polarimetry images for pathologist's labelling (indicated scale bar same for all images). For implementation see Code 1 [29].

Biomedical Optics EXPRESS

to contain enough pixels to enable reasonable statistics, but small enough to limit inclusion of pixels from neighbouring structures.

$$MAD \equiv \frac{\sum_{i=1}^{n-1}\sum_{j=i}^{n} B(i) - B(j)}{\frac{n(n-1)}{2}} \tag{4}$$

where n is the number of pixels in the sliding window and $B(x)$ is the birefringence orientation at pixel x. Here, x indicates the linear index of a pixel in the 5×5 sliding window.

Regions that have a low mean angular difference suggest that the local structures have similar axes of birefringence and are thus relatively aligned. As such, sclerotic regions are expected to exhibit lower MAD values compared to the more disorganized myxoid stroma areas. The final alignment score was calculated as the median MAD for a given ROI and then inverted, so as to have highly aligned regions correspond to high values of this metric.

2.5.3. Density (Fig. 2(f))

Lastly, the density of collagen fibers in a region is an important aspect of stromal architecture and often exhibits a significant difference between sclerotic and myxoid regions. To analyze this, traditionally the fibers must be segmented from the surrounding tissue structures and then their local density is quantified. Using the MIR image for this task is problematic, as the tissue birefringence magnitudes can vary, making segmentation challenging. To overcome this varying birefringence intensity challenge, an alternate approach based on a goodness-of-fit (R^2) metric was introduced. In our crossed-polarizer imaging methodology, a birefringent fiber will produce a sinusoidal intensity pattern when imaged over a range of polarizer angles as shown in Eq. (2). The goodness-of-fit between the observed intensity pattern and the theoretical dependence of Eq. (2) separates birefringent structures (which have a high fit value) from non-birefringent structures (which have intensity patterns that do not resemble Eq. (2)). Importantly, as the intensity signals are normalized before this calculation, the R^2 metric is independent of the MIR magnitude, making it well suited for the segmentation of birefringent collagen fibres. The R^2 metric is calculated by:

$$R^2 \equiv 1 - \frac{\sum_{z=1}^{Z}\left(y_{(i,j,z)} - f_{(i,j,z)}\right)}{\sum_{z=1}^{Z}\left(y_{(i,j,z)} - \bar{y}_{(i,j)}\right)} \tag{5}$$

where Z is the number of angular images, $y(i,j,z)$ indicates the brightness of a particular pixel at a given image z, $\bar{y}_{(i,j)}$ is the mean over all images at (i,j) and $f_{(i,j,z)}$ is the expected value as calculated by Eq. (2).

Using an empirically determined R^2 value of 0.75 as a threshold, birefringent fibers could be effectively segmented from the background. The collagenous stroma density is then calculated by a ratio of the number of pixels with fibers present ($R^2 > 0.75$) to the total number of pixels in the analyzed ROI.

$$\textit{Density}\ \text{Score} \equiv \frac{\#\textit{pixels with}\ R^2{>}0.75}{\textit{total}\ \#\ \text{pixels}} \tag{6}$$

2.5.4. Combined SAS image (Fig. 2(g))

Based on the properties of sclerotic and myxoid stroma and thus their expected differences, we introduce a quantitative signature whose value is directly proportional to the metrics of birefringent intensity, fiber alignment and fiber density within a given region. Therefore, we define the stromal architecture signature (SAS) metric to reflect this relationship:

$$SAS = Intensity \cdot Alignment \cdot Density \tag{7}$$

Several different combinations of the three constituent information channels, including weighted averages, were examined to determine if they added additional classification power. To a first

Biomedical Optics EXPRESS

approximation, the simple product of Eq. (7) exhibited the best results. As our understanding of the various elements of stromal morphology improves, the SAS definition may be modified to allow for certain features to be weighed in a more sophisticated manner.

2.6. Statistical tests

Intensity, alignment and density parameters, and subsequently the SAS, were calculated for each ROI. As a test of the separatory power of the SAS, we searched for a threshold value to distinguish ROIs as myxoid or sclerotic; this was set to be the highest non-outlier SAS value for myxoid (= 123, see Fig. 4(d) and discussion below). While suitable at this proof-of-principle stage, future work will examine generalizability and overfitting issues that may be present with such direct threshold selection. Initial efforts to assess this generalizability were done in the form of 5-fold cross-validation. That is, the dataset was separated into five groups of approximately equal size. A threshold was calculated using four of the five groups (as described above) and then had its performance tested on the fifth group. This was done five times (so each group was used as the testing set once) and performance metrics were noted for each trial.

Using the threshold $SAS_{th} = 123$, overlap between the two categories was determined and statistical agreement with the pathologist labelling was assessed using a two-sided Fisher's exact test. The null hypothesis for this test is that there is no significant difference between the populations of a 2×2 contingency table. Therefore, the common p-value threshold (<0.05 level) indicates that there are significant differences between the examined metric and the pathologist's classification (thus an unsuccessful metric); conversely, a higher p-value suggests a useful metric whose outcome agrees with the pathologist.

3. Results

Representative SAS images of each stromal category are shown in Fig. 3, together with adjacent histological H&E sections. Note the marked contrast between myxoid and sclerotic stroma in the SAS images, and a ~6X increase in SAS scores across the myxoid to sclerotic stromal categories. Analogous calculations to Fig. 3 were performed for all 96 ROIs (20 different patient samples) and grouped according to their true pathologist-assigned category labels. Figure 4 shows the outcome of this analysis.

As seen in Fig. 4(a)–(c), each individual score provides a modest separation between the sclerotic, mildly myxoid and myxoid categories, with significant overlaps. As expected, the inclusion of these three complimentary information channels of stromal abundance and morphology into the final SAS metric score results in significantly improved separation between all groups (Fig. 4(d)) – note that all ordinate axes in Fig. 4 are independently scaled to maximize data inclusion. Myxoid stroma, typically characterized by short, disorganized and sparse fibers, exhibits low SAS values relative to sclerotic regions with more fibrous, organized and dense stroma. Mildly myxoid regions occupy an intermediate position between myxoid and sclerotic ones and yield intermediate SAS scores. Figure 4(e) presents a quantitative summary table of the SAS results. The minimum, maximum and median statistics exclude outliers defined as lying greater than $\pm 2.7\sigma$ from the mean (outlier cases discussed below). Interestingly, in addition to larger separation between the three groups, the use of the SAS metric resulted in substantially reduced variance in the myxoid and mildly myxoid categories.

Apart from one outlier, all ROIs labelled as myxoid had SAS scores below 123. Using this simple threshold value may prove helpful for classification and segmentation, for example to rule out a particular region being myxoid (i.e., if SAS > 123, not myxoid). As this category is has been linked to more aggressive disease with worse prognosis, future work providing automatic assessment of breast cancer samples will prioritize the avoidance of false negatives in myxoid stroma classification. That is, the consequences of misclassifying a myxoid region as sclerotic

Biomedical Optics EXPRESS

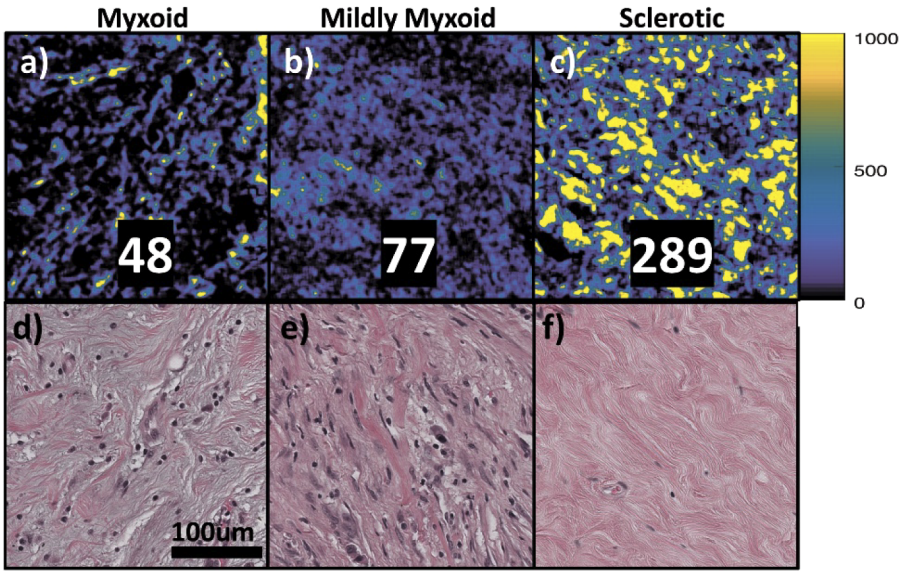

Fig. 3. A comparison of SAS parametric images (top row) and the resulting SAS scores with H&E histology (bottom row), for representative regions of the three stromal categories: a & d) = myxoid, b & e) = mildly myxoid and c & f) = sclerotic. The SAS scores, shown in white text, were computed for the entire regions shown in a), b) and c) respectively. Note the consistent trend of increasing SAS scores (higher values indicate more sclerotic stroma) and the pathologist assessment categories. The slightly lower resolution exhibited by the polarized light parametric images is due to 11×11 pixel sliding window used to calculate the SAS scores. Scale bar shown in d) is same for all images.

are potentially of greater clinical significance than the converse, as it could lead to an under treatment of aggressive disease.

Figure 5 further highlights the modest ability of individual metrics, and the improved performance of the composite SAS, to distinguish myxoid and sclerotic ROIs. Mildly myxoid category was omitted in this analysis, in order to report the agreement with the 'traditional' binary labelling system that served as the ground truth. As summarized in the figure caption, we used a simple threshold for the three individual metrics based on the same criteria as for SAS (the highest non-outlier SAS value for the myxoid class). For the myxoid classification, the SAS approach yielded the best result, with 97% sensitivity, 88% specificity and 91% total accuracy. The 5-fold cross-validation analysis yielded sensitivity of $94 \pm 8.5\%$, specificity of $88 \pm 5.4\%$ and an average total accuracy of $90 \pm 5.6\%$. By examining the Venn diagrams, particularly the proportion of the overlapping regions, the capabilities of the three distinct polarimetry metrics and the added value of their SAS composite can be visually appreciated.

To evaluate the statistical agreement between the two-class labelling performed by the PLM metrics (Fig. 5(a-d)) and the pathologist, a Fisher's exact test was used. Substantive differences were found for the intensity, alignment, and density metrics (p-values < 0.05, < 0.01, < 0.01 respectively), indicating statistically significant disagreements with the pathologist assessment. Conversely, the comparison between the SAS results and the pathologist yielded $p=0.52$, indicating similar performance.

Biomedical Optics EXPRESS

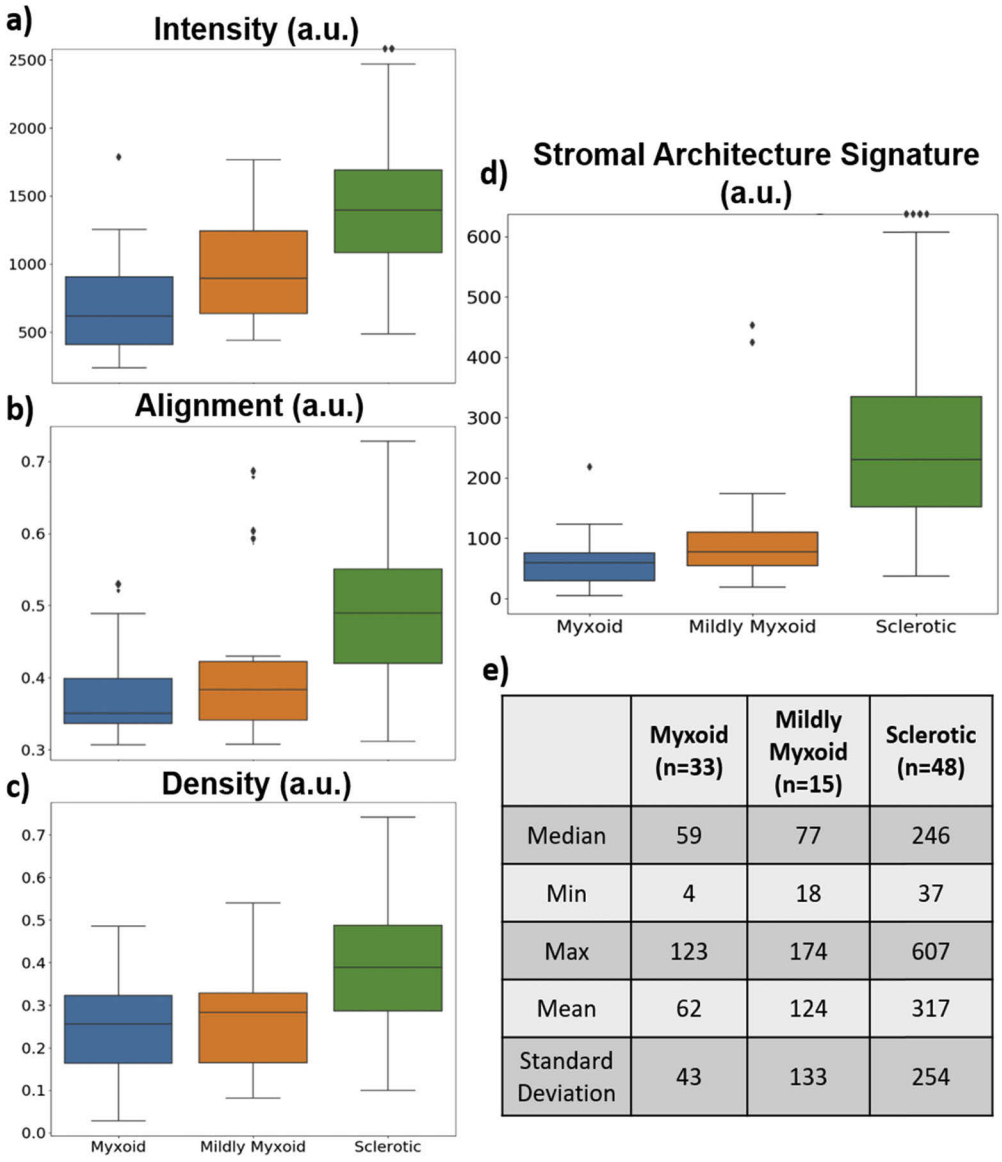

e)

	Myxoid (n=33)	Mildly Myxoid (n=15)	Sclerotic (n=48)
Median	59	77	246
Min	4	18	37
Max	123	174	607
Mean	62	124	317
Standard Deviation	43	133	254

Fig. 4. Box plots for the three intermediate metrics scores (left) and the final SAS score (right) calculated for each of the three pathologist-labelled categories for this study. For each box plot, the central line shows the mean, the box denotes the 2nd and 3rd quartiles, the whiskers indicate the 1st and 4th quartile respectively, and outliers are demarcated by symbols. Outliers on the top border of a graph indicate that they occur above the maximum value on the axes but were compressed to enable visualization. a) Intensity scores b) Alignment scores c) Density scores d) SAS scores. e) Table showing the SAS summary statistics. The median corresponds to the position of the central line in d), while min and max correspond to the positions of the bottom and top whiskers respectively; mean and standard deviation were calculated with outliers included. Of note is the greater separation between myxoid and sclerotic classes after incorporation all three metrics into the SAS score, as well as the significant reduction in variance of the myxoidal categories as seen in d).

Biomedical Optics EXPRESS

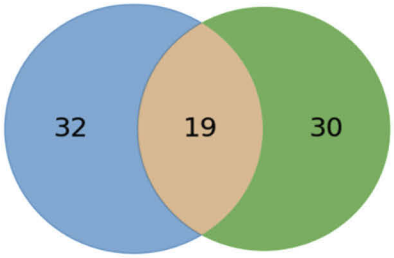

	Predicted Myxoid	Predicted Sclerotic
True Myxoid	32	1
True Sclerotic	18	30

b) Alignment

	Predicted Myxoid	Predicted Sclerotic
True Myxoid	32	1
True Sclerotic	24	24

c) Density

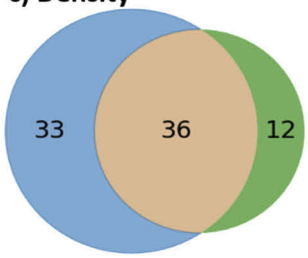

	Predicted Myxoid	Predicted Sclerotic
True Myxoid	33	0
True Sclerotic	36	12

d) SAS

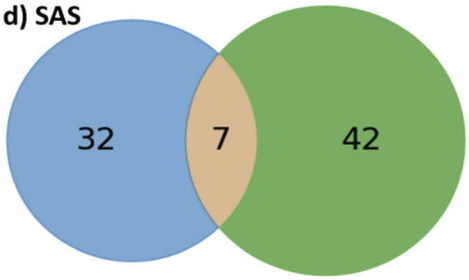

	Predicted Myxoid	Predicted Sclerotic
True Myxoid	32	1
True Sclerotic	6	42

e)

	Sensitivity (%)	Specificity (%)	Total Accuracy (%)
a) Intensity	97	63	76
b) Alignment	97	50	69
c) Density	100	25	55
d) SAS	**97**	**88**	**91**

Fig. 5. A visual and numerical representation of the overlap (orange) between myxoid (blue) and sclerotic (green) ROIs classified by a) Intensity b) Alignment c) Density and d) SAS scores. The numbers in the blue and green circles are the amounts of correctly identified myxoid and sclerotic ROIs respectively; those in the middle orange regions indicate the misclassifications, or, overlap of the two groups. Of particular interest is the substantially improved separation afforded by the SAS score d), compared to any of the individual a) – c) metrics. Alongside each Venn diagram is a confusion matrix displaying the correct classifications (blue and green) and the misclassifications (orange). e) Table indicating the sensitivity, specificity and total accuracy of each of the metrics and the composite SAS. The thresholds were as follows: Intensity = 1255, Alignment = 0.490, Density = 0.486 and SAS = 123, each calculated to maximize the sensitivity to myxoid stroma. Note the resultant poor specificity and total accuracy for each of the individual metrics, and the significantly better SAS results.

Biomedical Optics EXPRESS

4. Discussion

We have developed a novel methodology to assess and quantify architectural patterns of fibrillar stroma in the tumor microenvironment, using polarized light imaging in a cohort of invasive ductal carcinoma surgical breast cancer specimens. We also demonstrated that the developed signature from this methodology has excellent ability to classify the stroma as myxoid versus sclerotic when compared against the pathologist assessment. The PLM method of scoring stromal architecture uses three distinct polarimetrically-derived quantitative images containing morphological information (intensity, alignment and density) in order to provide a composite SAS score. This score is quantitative and furnishes a continuous numerical spectrum that potentially reflects the wide range of stromal morphologies, over and above the broad myxoid and sclerotic categories. Importantly, the method is objective and pathologist invariant, resulting in robust and readily reproducible objective results. By using a simple threshold ($SAS_{th} = 123$), we obtained 97% sensitivity, 88% specificity and 91% accuracy for myxoid stroma detection.

Figure 6 illustrates the shortcomings of the current binary classification approach, specifically the wide spectrum of architectural morphologies within the myxoid and sclerotic tumoral stroma not captured in this broad 2-class categorization. Given the apparent difference in morphology between region (c) and (d), one could hypothesize that their structure would predict different tumor behavior or patient outcomes despite both being categorized as sclerotic stroma using the current H&E based pathology approaches. However, using the SAS one is able to readily and clearly separate these two sclerotic stroma samples (SAS values of 158 and 814, respectively) and study their potential difference in clinical behavior. This is information that is lost with the traditional binary and subjective method of classification. Conversely, examining regions (b) and (c) one may appreciate similarities in their morphology even though they are classified into two separate, pathologist-labelled categories; these similarities are reflected in their relatively closer SAS scores (103 and 158, respectively). These observations question the accuracy and utility of the subjective binary classification scheme, and suggest a more insightful, objective and nuanced stromal quantification is afforded by our methodology. In light of the recent emphasis on mining the TME for useful prognosticators and treatment guides [8,9,11], the current subjective and over-simplified system of labelling may inhibit future efforts to reproducibly probe the role of the stroma in breast cancer.

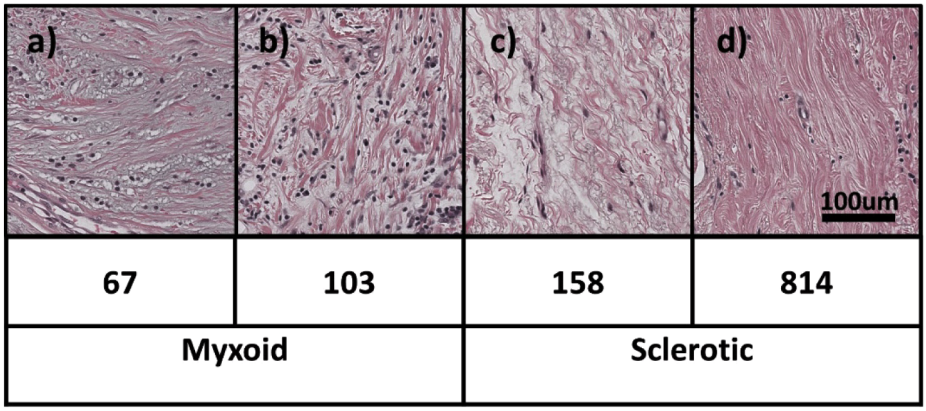

Fig. 6. H&E stained IDC sample slides labelled as a) highly myxoid b) slightly myxoid c) slightly sclerotic d) highly sclerotic by a pathologist. Calculated SAS scores are shown in the middle row, and overall pathologist classification categories are on the bottom. Of particular interest is the continuous numerical SAS spectrum of stromal signatures, potentially more informative than the binary two-broad-categories subjective approach currently employed in pathology.

Biomedical Optics EXPRESS

As shown in Fig. 5, a simple empirically determined threshold of $SAS_{th} = 123$ was sufficient to yield excellent classification power between myxoid and sclerotic stroma as compared to the gold standard of pathologist's assessment. A recent report of automatic assessment of stromal maturity yielded an accuracy of 84% [30]; our SAS result of 91% compares very well to this finding. Encouragingly, the results presented here demonstrated the excellent separatory power afforded by the SAS, which relied solely on a simple threshold, and could likely be improved by employing more advanced machine learning methods that have recently emerged as useful tools for histopathological analysis [31,32]. Future efforts will be put towards exploring these options as well as moving to whole-slide processing to avoid the need for ROI selection. Further, different strategies of defining the governing SAS metric from constituent images [Eq. (7)] will also be explored.

Another noteworthy finding is the different range of SAS values within the sclerotic and myxoid groups. Regions of myxoid stroma are significantly less heterogeneous in terms of their morphological presentation as compared to sclerotic stroma. Figure 4 demonstrates this difference in organization between the two groups, with the range of sclerotic SAS values being ~5X greater than the myxoid range. This observation may or may not have a clinical or biological significance but seems to be absent from the literature. The quantitative nature of the SAS enables future work to better understand these differences and assess their significance. Interesting questions such as this would likely not arise, nor be potentially answerable, using the current subjective and categorical binary classification techniques.

As with any new methodology, the most informative cases for its refinement may be the "mistakes". We attribute the few SAS misclassifications (n=7 out of 96 ROIs) to two main causes: edema and elastin. Illustrative examples of these are presented in Fig. 7. Edematous regions (Fig. 7(a), red box) are characterized by well-defined collagen fibers that are separated by interstitial fluid. Despite the fibers appearing bright on the intensity images, the lower density of the fibers resulted in SAS values below the separating threshold. Although misclassified compared to the pathologist's labelling, the lower SAS score captures the clear difference that one can readily appreciate by comparing the H&E for sclerotic stroma with (Fig. 7(a), red box) and without edema (Fig. 7(c), black box).

Occasional SAS misclassification also seems to arise from the presence of elastin. Despite often appearing fibrillar in nature, elastin is only very weakly birefringent [33] and thus does not produce significant polarimetric contrast. The region demarcated with the red square in Fig. 7(c) and (d) shows this lack of polarimetric signal from elastin. While in some sense this is a limitation, the insensitivity of the PLM method to non-birefringent structures makes it well suited for the study of collagenous stroma.

A potential shortfall of a myxoid – sclerotic "ground-truth" determined by a single pathologist is the problem of inter-pathologist variability. Inter-pathologist categorization of myxoidal stroma architecture is often quantified with a Krippendorf's Alpha test which can range from 1 (perfect agreement between observers) to 0 (agreement comparable to random chance). Previous studies have found inter-pathologist agreements to be poor (in the range of KA = 0.45) [34,35] on classifying stromal architecture. However, these studies examined full slides and asked for a categorical assessment of the abundance of myxoid stroma (i.e. low < 10% myxoid, intermediate <30%, etc). Here, we have attempted to limit this issue by the use of smaller 200×200μm regions of interest specifically examining stromal areas. Future studies will have additional pathologists to further explore the effects of this variability in the determination of the "ground truth". That said, the known suboptimal inter-observer variability in assessment of stroma architecture underscores the need for technological advancements, such as our proposed objective methodology, that can complement and potentially improve the pathologists' examinations.

As alternatives to the proposed polarimetric methodology for stromal assessment, other methods of connective tissue characterization may be considered. Second harmonic generation

Biomedical Optics EXPRESS

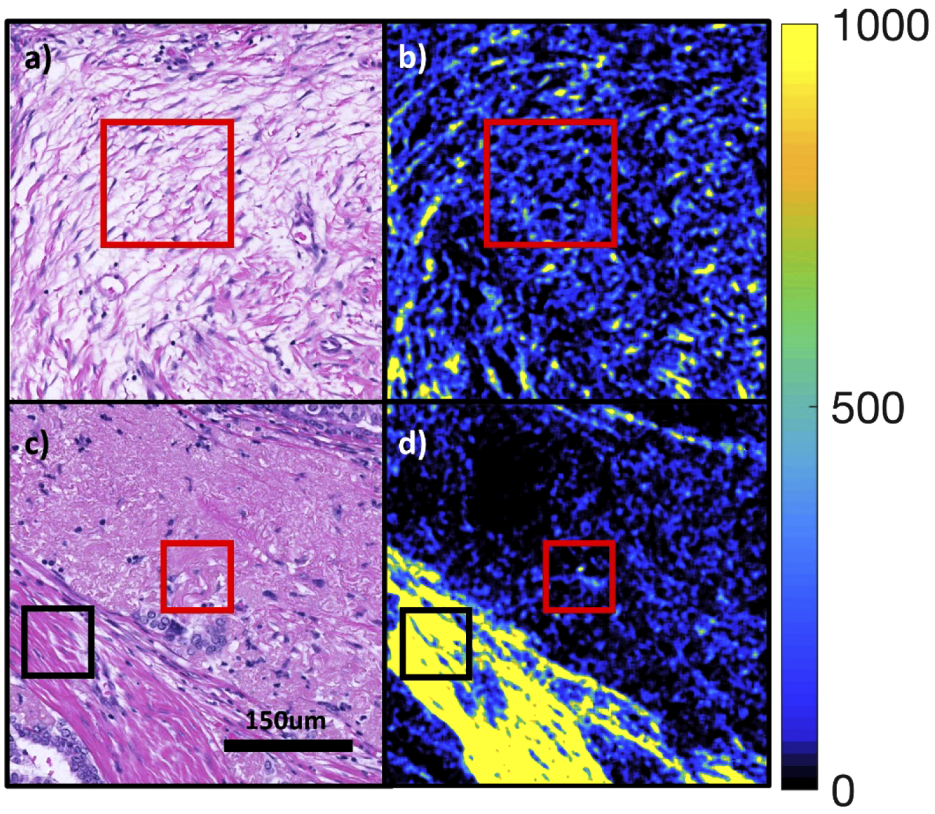

Fig. 7. Comparison of the H&E and SAS parametric images for two pathology-categorized sclerotic regions that were SAS-misclassified as myxoid. a, b) A region of edematous collagen (red box), labelled sclerotic by a pathologist but SAS-misidentified as myxoid. Although the brightness of the fibers would suggest the correct (sclerotic) class, the relatively low density reduces the resultant SAS score to the myxoid levels. c, d) A region containing elastin (red box) that was erroneously identified as myxoid by its SAS score. For comparison, note high SAS values shown for the collagen region (black box). Scale is the same across all images.

(SHG) is one such method extensively used in research [36–38] and is currently considered the gold standard for collagen imaging. SHG, however, needs a femtosecond laser and an advanced microscope. The high cost and the technical expertise required to maintain it may not be feasible for many institutions. Additionally, imaging time required for a single 200 X 200 μm^2 (512px X 512px) region of interest is at least 15min [39]. Conversely, the described PLM technique can image a 1.6 X 1.6mm^2 region at comparable resolution (2048px X 2048px) in under 3min and can be significantly improved (tens of seconds) with a brighter light source (shorter exposure times) and refined rotation timing. Unlike SGH, the simple nature of the PLM modular optics enables direct incorporation into existing commercial microscopes. Coupled with robust signal processing and image analysis, as described, the methodology of obtaining SAS scores should thus be easily implementable into both research settings and current pathology workflows. For the latter scenario, it is of note that the automated nature of the image processing combined with the availability of the software (see Code 1 [29]) will ensure that scores can be computed without direct pathologist oversight.

Biomedical Optics EXPRESS

Picrosirius red (PSR) staining is another alternative approach to collagen morphology analysis. Recent studies have investigated stromal architecture using PSR-stained human DCIS breast cancer cores and demonstrated that stromal characteristics were predictive of recurrence risk [40]. While imaging and analysis of stained slides is promising, the process of fixing and staining is labor intensive, time consuming and can alter tissue properties irreversibly. While these procedures are inevitable in the current pathology assessment workflow, their various artefacts can create serious obstacles in computationally based classification systems [41]. Therefore, a method that works on unstained, fresh tissues such as our proposed PLM SAS approach (see Code 1 [29]) can avoid these artefactual complications. Furthermore, the avoidance of tissue fixing, imbedding and staining are advantageous for potential use in intraoperative settings [42,43].

5. Conclusions

Currently, there is no histopathological standard for providing a quantitative, objective characterization of the stromal morphology in a patient's tumor. Here we present a polarized light-based method that addresses this unmet clinical need and yields a continuous score capable of quantitatively representing the range of varying and complex stromal architectures. The resultant stromal architecture signature (SAS) was compared to pathologist labelling of human intraductal carcinoma breast cancer samples and excellent agreement was found. Refinements of the presented methodology that can further improve its performance were outlined. The novel PLM approach used to generate the informative stromal images is simple and compatible with many commercial microscopes, enabling potential adoption for breast cancer examinations and for many other types of solid tumors where the importance of the TME appears established. As the role of the stroma in prognostication and possibly treatment planning becomes more pronounced, such operator-independent, objective, and quantitative stromal characterization tool will be needed. Further validation studies probing the link between polarimetrically assessed stromal morphology and clinical disease characteristics need to be performed and are currently commencing in our laboratory. The ensuing reduction of methodological variance in future stromal quantification studies may elucidate robust connections between structure and function as it relates to tumors of various types, their microenvironment and patient outcomes.

Funding

Natural Sciences and Engineering Research Council of Canada (410009540); Canadian Institutes of Health Research (PJT-156110).

Disclosures

The authors declare no conflicts of interest.

References

1. F. Bray, J. Ferlay, I. Soerjomataram, R. L. Siegel, L. A. Torre, and A. Jemal, "Global cancer statistics 2018: GLOBOCAN estimates of incidence and mortality worldwide for 36 cancers in 185 countries," Ca-Cancer J. Clin. **68**(6), 394–424 (2018).
2. A. Matikas, T. Foukakis, S. Swain, and J. Bergh, "Avoiding over-and undertreatment in patients with resected node-positive breast cancer with the use of gene expression signatures: are we there yet?" Ann. Oncol. **30**(7), 1044–1050 (2019).
3. M. G. Wallis, "How do we manage overdiagnosis/overtreatment in breast screening?" Clin. Radiol. **73**(4), 372–380 (2018).
4. I. Krop, N. Ismaila, F. Andre, R. C. Bast, W. Barlow, D. E. Collyar, and R. G. Mennel, "Use of biomarkers to guide decisions on adjuvant systemic therapy for women with early-stage invasive breast cancer: American Society of Clinical Oncology clinical practice guideline focused update," J. Clin. Oncol. **35**(24), 2838–2847 (2017).
5. M. B. Hannouf, G. S. Zaric, P. Blanchette, C. Brezden-Masley, M. Paulden, C. McCabe, and M. Brackstone, "Cost-effectiveness analysis of multigene expression profiling assays to guide adjuvant therapy decisions in women with invasive early-stage breast cancer," Pharmacogenomics J. **20**(1), 27–46 (2020).

Biomedical Optics EXPRESS

6. C. B. Weldon, J. R. Trosman, W. J. Gradishar, A. B. Benson III, and J. C. Schink, "Barriers to the use of personalized medicine in breast cancer," J. Oncol. Pharm. Pract. **8**(4), e24–e31 (2012).
7. M. W. Conklin and P. J. Keely, "Why the stroma matters in breast cancer: insights into breast cancer patient outcomes through the examination of stromal biomarkers," Cell Adhes. Migr. **6**(3), 249–260 (2012).
8. D. Hanahan and L. M. Coussens, "Accessories to the crime: functions of cells recruited to the tumor microenvironment," Cancer Cell **21**(3), 309–322 (2012).
9. M. R. Junttila and F. J. de Sauvage, "Influence of tumour micro-environment heterogeneity on therapeutic response," Nature **501**(7467), 346–354 (2013).
10. L. A. Liotta, P. S. Steeg, and W. G. Stetler-Stevenson, "Cancer metastasis and angiogenesis: an imbalance of positive and negative regulation," Cell **64**(2), 327–336 (1991).
11. M. M. Mueller and N. E. Fusenig, "Friends or foes - Bipolar effects of the tumour stroma in cancer," Nat. Rev. Cancer **4**(11), 839–849 (2004).
12. B. U. Pauli, D. E. Schwartz, E. J. M. Thonar, and K. E. Kuettner, "Tumor invasion and host extracellular matrix," Cancer Metastasis Rev. **2**(2), 129–152 (1983).
13. E. M. de Kruijf, J. G. H. van Nes, C. J. H. van de Velde, H. Putter, V. T. Smit, G. J. Liefers, and W. E. Mesker, "Tumor–stroma ratio in the primary tumor is a prognostic factor in early breast cancer patients, especially in triple-negative carcinoma patients," Breast Cancer Res. Treat. **125**(3), 687–696 (2011).
14. C. L. Downey, S. A. Simpkins, J. White, D. L. Holliday, J. L. Jones, L. B. Jordan, and V. Speirs, "The prognostic significance of tumour-stroma ratio in oestrogen receptor-positive breast cancer," Br. J. Cancer **110**(7), 1744–1747 (2014).
15. C. L. Downey, H. H. Thygesen, N. Sharma, and A. M. Shaaban, "Prognostic significance of tumour stroma ratio in inflammatory breast cancer," SpringerPlus **4**(1), 68 (2015).
16. F. J. A. Gujam, J. Edwards, Z. M. A. Mohammed, J. J. Going, and D. C. McMillan, "The relationship between the tumour stroma percentage, clinicopathological characteristics and outcome in patients with operable ductal breast cancer," Br. J. Cancer **111**(1), 157–165 (2014).
17. C. J. H. Kramer, K. M. H. Vangangelt, G. W. van Pelt, T. J. A. Dekker, R. Tollenaar, and W. E. Mesker, "The prognostic value of tumour–stroma ratio in primary breast cancer with special attention to triple-negative tumours: a review," Breast Cancer Res. Treat. **173**(1), 55–64 (2019).
18. P. Aurello, G. Berardi, D. Giulitti, A. Palumbo, S. M. Tierno, G. Nigri, and G. Ramacciato, "Tumor-Stroma Ratio is an independent predictor for overall survival and disease free survival in gastric cancer patients," The Surg. **15**(6), 329–335 (2017).
19. J. Liu, J. Liu, J. Li, Y. Chen, X. Guan, X. Wu, and X. Wang, "Tumor–stroma ratio is an independent predictor for survival in early cervical carcinoma," Gynecol. Oncol. **132**(1), 81–86 (2014).
20. W. E. Mesker, J. Junggeburt, K. Szuhai, P. de Heer, H. Morreau, H. J. Tanke, and R. A. E. M. Tollenaar, "The carcinoma–stromal ratio of colon carcinoma is an independent factor for survival compared to lymph node status and tumor stage," Anal. Cell. Pathol. **29**(5), 387–398 (2007).
21. S. Ahn, J. Cho, J. Sung, J. E. Lee, S. J. Nam, K.-M. Kim, and E. Y. Cho, "The prognostic significance of tumor-associated stroma in invasive breast carcinoma," Tumor Biol. **33**(5), 1573–1580 (2012).
22. C. Jing, Y. Fu, J. Huang, M. Zhang, Y. Yi, W. Gan, and S. Zheng, "Prognostic nomogram based on histological characteristics of fibrotic tumor stroma in patients who underwent curative resection for intrahepatic cholangiocarcinoma," Oncologist **23**(12), 1482–1493 (2018).
23. H. Ueno, A. M. Jones, K. H. Wilkinson, J. R. Jass, and I. C. Talbot, "Histological categorisation of fibrotic cancer stroma in advanced rectal cancer," Gut **53**(4), 581–586 (2004).
24. M. Van Bockstal, K. Lambein, A. Smeets, L. Slembrouck, P. Neven, I. Nevelsteen, and C. Van Ongeval, "Stromal characteristics are adequate prognosticators for recurrence risk in ductal carcinoma in situ of the breast," Eur. J. Surg. Oncol. **45**(4), 550–559 (2019).
25. L. M. Wang, M. A. Silva, Z. D'Costa, R. Bockelmann, Z. Soonawalla, S. Liu, and R. Muschel, "The prognostic role of desmoplastic stroma in pancreatic ductal adenocarcinoma," Oncotarget **7**(4), 4183–4194 (2016).
26. Y. Dong, J. Qi, H. He, C. He, S. Liu, J. Wu, D. S. Elson, and H. Ma, "Quantitatively characterizing the microstructural features of breast ductal carcinoma tissues in different progression stages by Mueller matrix microscope," Biomed. Opt. Express **8**(8), 3643–3655 (2017).
27. J. Westreich, M. Khorasani, B. Jones, V. Demidov, S. Nofech-Mozes, and A. Vitkin, "Novel methodology to image stromal tissue and assess its morphological features with polarized light: towards a tumour microenvironment prognostic signature," Biomed. Opt. Express **10**(8), 3963–3973 (2019).
28. M. F. G. Wood, N. Vurgun, M. A. Wallenburg, and I. A. Vitkin, "Effects of formalin fixation on tissue optical polarization properties," Phys. Med. Biol. **56**(8), N115–N122 (2011).
29. B. Jones "Stromal Architecture Signature Repository", *Code Repository* (2020), https://github.com/blakempjones/StromalArchitectureSignature
30. S. Reis, P. Gazinska, J. H. Hipwell, T. Mertzanidou, K. Naidoo, N. Williams, and D. J. Hawkes, "Automated classification of breast cancer stroma maturity from histological images," IEEE Trans. Biomed. Eng. **64**(10), 2344–2352 (2017).
31. Ł. Rączkowski, M. Możejko, J. Zambonelli, and E. Szczurek, "ARA: accurate, reliable and active histopathological image classification framework with Bayesian deep learning," Sci. Rep. **9**(1), 14347 (2019).

Biomedical Optics EXPRESS

32. Y. Rivenson, H. Wang, Z. Wei, K. de Haan, Y. Zhang, Y. Wu, and A. E. Sisk, "Virtual histological staining of unlabelled tissue-autofluorescence images via deep learning," Nat. Biomed. Eng. **3**(6), 466–477 (2019).
33. B. B. Aaron and J. M. Gosline, "Optical properties of single elastin fibres indicate random protein conformation," Nature **287**(5785), 865–867 (1980).
34. H. Dano, et. al, "Interobserver variability in upfront dichotomous histopathological assessment of ductal carcinoma in situ of the breast: the DCISion study," Mod. Pathol. **33**(3), 354–366 (2020).
35. M. Van Bockstal, M. Baldewijns, C. Colpaert, H. Dano, G. Floris, C. Gallant, K. Lambein, D. Peters, S. Van Renterghem, A.-S. Van Rompuy, S. Verbek, S. Verschuere, and J. Van Dorpe, "Dichotomous histopathological assessment of ductal carcinoma in situ of the breast results in substantial interobserver concordance," Histopathology **73**(6), 923–932 (2018).
36. M. W. Conklin, J. C. Eickhoff, K. M. Riching, C. A. Pehlke, K. W. Eliceiri, P. P. Provenzano, and P. J. Keely, "Aligned collagen is a prognostic signature for survival in human breast carcinoma," Am. J. Pathol. **178**(3), 1221–1232 (2011).
37. P. P. Provenzano, K. W. Eliceiri, J. M. Campbell, D. R. Inman, J. G. White, and P. J. Keely, "Collagen reorganization at the tumor-stromal interface facilitates local invasion," BMC Med. **4**(1), 38 (2006).
38. P. P. Provenzano, D. R. Inman, K. W. Eliceiri, J. G. Knittel, L. Yan, C. T. Rueden, and P. J. Keely, "Collagen density promotes mammary tumor initiation and progression," BMC Med. **6**(1), 11 (2008).
39. X. Chen, O. Nadiarynkh, S. Plotnikov, and P. J. Campagnola, "Second harmonic generation microscopy for quantitative analysis of collagen fibrillar structure," Nat. Protoc. **7**(4), 654–669 (2012).
40. M. S. Toss, I. M. Miligy, K. L. Gorringe, A. AlKawaz, K. Mittal, R. Aneja, and E. A. Rakha, "Geometric characteristics of collagen have independent prognostic significance in breast ductal carcinoma in situ: an image analysis study," Mod. Pathol. **32**(10), 1473–1485 (2019).
41. R. Bhargava and A. Madabhushi, "Emerging themes in image informatics and molecular analysis for digital pathology," Annu. Rev. Biomed. Eng. **18**(1), 387–412 (2016).
42. R. Laucirica, "Intraoperative assessment of the breast: guidelines and potential pitfalls," Arch. Pathol. Lab. Med. **129**(12), 1565–1574 (2005).
43. B. W. Maloney, D. M. McClatchy, B. W. Pogue, K. D. Paulsen, W. A. Wells, and R. J. Barth, "Review of methods for intraoperative margin detection for breast conserving surgery," J. Biomed. Opt. **23**(10), 1 (2018).